Lattice-Strain Control of Exceptional Activity in Dealloyed Core-Shell Fuel Cell Catalysts

Peter Strasser*[1,2], Shirlaine Koh[1], Toyli Anniyev[3,4], Jeff Greeley[5], Karren More[6], Chengfei Yu[1], Zengcai Liu[1], Sarp Kaya[3,4], Dennis Nordlund[4], Hirohito Ogasawara[3,4], Michael F. Toney[3,4] and Anders Nilsson[3,4]

[1]Department of Chemical and Biomolecular Engineering, University of Houston, Houston, TX 77204, USA

[2] Department of Chemistry, Chemical Engineering Division, Technical University Berlin, 10623 Berlin, Germany

[3] Stanford Institute of Materials and Energy Sciences, SLAC National Accelerator Laboratory, Menlo Park, CA 94025, USA

[4] Stanford Synchrotron Radiation Lightsource, SLAC National Accelerator Laboratory, Menlo Park, CA 94025, USA

[5]Center for Nanoscale Materials, Argonne National Laboratory, Argonne, IL , 60439, USA

[6] Materials Science & Technology Division,ʼ Oak Ridge National Laboratory, Oak Ridge, TN 37831-6064, USA

Abstract

We present a combined experimental and theoretical approach to demonstrate how lattice strain can be used to continuously tune the catalytic activity of the oxygen reduction reaction (ORR) on bimetallic nanoparticles that have been dealloyed. The sluggish kinetics of the ORR is a key barrier to the adaptation of fuel cells and currently limits their widespread use. Dealloyed Pt-Cu bimetallic nanoparticles, however, have been shown to exhibit uniquely high reactivity for this reaction. We first present evidence for the formation of a core-shell structure during dealloying, which involves removal of Cu from the surface and subsurface of the precursor nanoparticles. We then show that the resulting Pt-rich surface shell exhibits compressive strain that depends on the composition of the precursor alloy. We next demonstrate the existence of a downward shift of the Pt d-band, resulting in weakening of the bond strength of intermediate oxygenated species due to strain. Finally, we combine synthesis, strain, and catalytic reactivity in an experimental/theoretical reactivity-strain relationship which provides guidelines for the rational design of strained oxygen reduction electrocatalysts. The stoichiometry of the precursor, together with the dealloying conditions, provides experimental control over the resulting surface strain and thereby allows continuous tuning of the surface electrocatalytic reactivity – a concept that can be generalized to other catalytic reactions.

Electrocatalytic energy conversion processes are expected to play a major role in the development of sustainable technologies to mitigate global warming and to lower our dependence on fossil fuels. More specifically, the Polymer Electrolyte Membrane fuel cell (PEMFC), an electrochemical energy conversion device, is potentially useful as a power source in the transportation sector, one of the largest sources of greenhouse gases and consumers of fossil fuels. Efficient and stable fuel cell electrocatalysts, however, are largely lacking[1-3], and, therefore, fundamental progress in the design of these catalysts is needed.

The ultimate goal in catalytic design is to have complete synthetic control of the material properties that determine the reactivity[4, 5]. Catalysts consisting of two metals (bimetallic) allow higher reactivity and more flexible design and have been the focus of recent studies [6-14]. There are three fundamental effects in bimetallic catalysis: *ensemble* effects, *ligand* effects, and *geometric* effects. Ensemble effects arise when dissimilar surface atoms, individually or in small groups (ensembles), take on distinct mechanistic functionalities, as demonstrated for Pd atom pairs on Au for a gas-phase catalytic reaction[7, 15]. Ligand effects are caused by the atomic neighborhood of two dissimilar surface metal atoms inducing electronic charge transfer between the atoms, thus affecting their electronic band structure. Finally, geometric effects are differences in reactivity based on the atomic arrangement of surface atoms and may include compressed or expanded arrangements of surface atoms (surface strain)[16]. Ligand and geometric effects [1, 2, 8, 15, 17-20] and, in some cases, all three effects[15], are generally simultaneously present and co-impact the observed catalytic reactivity. To date, however, no effective strategy for isolating and tuning strain effects in electrocatalytic systems has been realized. Considering the effective length scale where ensemble, geometric strain, and ligand effects are important, only geometric strain can impact surface reactivity over more than a few atomic layers. Hence, a catalyst structure consisting of a few atomic monometallic layers, supported on a substrate with different lattice parameter (a core-shell structure), should isolate geometric strain effects. If the amount of strain in these structures can be controlled we could, thereby, leverage the rich effects of bimetallic catalysis to continuously tune surface catalytic reactivity.

Dealloying is the preferential dissolution of the electrochemical more reactive component from a bimetallic alloy (precursor) consisting of a less reactive (here Pt) and more reactive metal (here Cu)[21-23]. We have shown that dealloyed Pt-Cu nanoparticles show uniquely high catalytic reactivity for the oxygen reduction reaction (ORR) in fuel cell electrodes[24-28] which is of tremendous importance, since it occurs at the cathode of virtually all fuel cells[29, 30], with pure Pt being the preferred catalyst. The ORR is sluggish, which is why significant amounts of Pt metal are required in fuel cells, making them prohibitively expensive. Dealloyed Pt catalysts, however, meet and exceed the technological activity targets in realistic fuel cells[24] as shown in Fig. S1 in the supplementary information (SI). Owing to their reactivity, dealloyed Pt catalysts can reduce the required amount of Pt by more than 80%. Despite this importance, the mechanistic origin of their enhanced reactivity remains poorly understood. To have hope of realizing similar property improvements for related electrocatalytic systems, underlying principles of their performance must be elucidated. Below, we demonstrate that the concept of strain tuning of the catalytic properties, introduced above, provides such a unifying principle.

Results

We studied six different Pt-Cu alloy nanoparticle precursors and their corresponding dealloyed counterparts. The alloy precursors varied in their initial atomic Pt-to-Cu ratio and in their preparation, in particular the annealing temperature. We will focus on two sets of three Pt-to-Cu ratios ($Pt_{25}Cu_{75}$, $Pt_{50}Cu_{50}$, $Pt_{75}Cu_{25}$); one set was annealed at 800 °C and the other at 950 °C. To obtain the active dealloyed catalysts, precursors were subjected to an identical electrochemical dealloying protocol where Cu was preferentially removed from the precursor particles.

We first address the structure of the Pt-Cu bimetallic precursors and the corresponding dealloyed catalysts. These form face-centered-cubic (fcc) disordered alloys[31]. In Fig. 1A and 1B we present energy-dispersive elemental color map overlays for Pt and Cu acquired using a probe-corrected Scanning Transmission Electron

Microscope (STEM) for the $Pt_{25}Cu_{75}$ / 800 °C alloy precursor and dealloyed catalyst, respectively; the mean particle size prior to dealloying (Fig. 1A) is around 4.5 nm (see histogram Fig. S2E), while the dealloyed, catalytically active form (Fig. 1D), exhibited a decrease in the average particle size to ~3.4 nm. The corresponding $Pt_{25}Cu_{75}$ / 950 °C alloy precursor and dealloyed catalysts showed average particle sizes of 6.0 nm and 5.1 nm, respectively. As Fig. 1B shows, for the dealloyed catalyst, the Cu is confined to the center of a majority of the dealloyed Pt-Cu nanoparticles. The dealloyed particles exhibit a distinct Pt-enriched layer (blue in Fig. 1B) on the surfaces of the alloy Pt-Cu cores (pink in Fig. 1B). A corresponding Energy Dispersive Spectroscopy (EDS) line profile taken across the diameter of typical (~4nm) dealloyed nanoparticle confirm the presence of a ~0.6nm Pt-enriched layer on the surface of the dealloyed particles (Fig. 1C). Hence, the Pt and Cu elemental maps and line profiles of Fig. 1 provide evidence for the formation of a core-shell structure in the nanoparticles following dealloying, where a Pt-enriched shell surrounds a Pt-Cu core. In addition, aberration-corrected high-angle annular dark-field STEM images indicate a change in the Pt and Cu distributions within the nanoparticles, from a uniform Pt-Cu alloy (Fig. 1D) to a morphology indicative of a core-shell structure (Fig. 1E)[32]. Further evidence comes from X-ray photoelectron spectroscopy (XPS) data that show a large enhancement of the surface concentration of Pt, see Table 1. Based on the STEM, EDS and XPS data, we estimate the thickness of the Pt-shell to be 0.6 - 1 nm, corresponding to 3 or more Pt rich layers, consistent with estimates from Anomalous Small Angle X-ray Scattering (ASAXS) of similar materials[33]. Because of the propensity for Cu to dissolve, dealloyed $Pt_{50}Cu_{50}$ and $Pt_{75}Cu_{25}$ nanoparticles will possess a similarly Pt enriched shell structure. From these combined, consistent results, we conclude that the geometry of the dealloyed Pt-enriched shell on the Pt-Cu core leads to the high electrocatalytic activity. Specifically, we hypothesize that lattice strain in the Pt shell controls the surface catalytic reactivity.

We address our lattice strain hypothesis using Anomalous X-ray diffraction (AXRD) which permits the independent measurement of the average lattice parameter and average composition of the scattering nanoparticles before and after dealloying. In AXRD diffraction patterns are collected at a number of X-ray energies near the X-ray absorption edge of an element of interest, here Cu. Fig. 2A shows (111) diffraction

profiles of a $Pt_{25}Cu_{75}$ precursor at several energies. Since the scattering power of Cu drops near the Cu absorption edge, the diffracted intensity of the alloy shows a characteristic decrease, as indicated by the arrow in Fig. 2A. In AXRD, peak positions yield average nanoparticle lattice parameters, while the relationship between scattering intensity and energy (equation S2) provides the chemical composition of the scattering alloy phase. As illustrated in Fig. 2B, the model equation (S2) for diffraction intensity (black line) was fitted to the integrated (111) peak intensities (red circles), and the compositions x_{Pt} and x_{Cu} were determined.

Given the core-shell nature of the dealloyed particles, the lattice strain in the Pt shell is most relevant for surface catalysis. To estimate the lattice parameter in the particle shell, we approximated the structure of the dealloyed particles by a simple two-phase core-shell model as depicted schematically in Fig. 2C. We assumed a pure Pt shell with lattice parameter a_{shell} surrounding a Pt-Cu alloy core with lattice parameter a_{core}. Using the AXRD derived nanoparticle compositions and lattice parameter data [34-36], our core-shell model allows for determination of a_{shell} and the strain s(Pt) in the particle shell relative to bulk Pt, $s(Pt) = \dfrac{a_{shell} - a_{Pt}}{a_{Pt}} \times 100$, where a_{Pt} is the bulk Pt lattice parameter.

Figure 2D shows a_{shell} as function of precursor composition and preparation temperature, while s(Pt) is shown in SI Figure S4. Foremost, the data show that for all catalysts the lattice parameter of the Pt shell, a_{shell} , is smaller than that of pure Pt (dotted line) – so compressively strained. With increasing Cu in the alloy precursor and with higher preparation temperature, a_{shell} becomes smaller and the magnitude of s(Pt) larger. The observed synthesis-strain trends are understood within our core-shell model. The lattice mismatch between the Pt shell and the Pt-Cu core causes a reduced Pt-Pt interatomic distance in the shell. The richer in Cu the particle core, the smaller its lattice parameter, and hence the more strain induced in the shell. A similar argument holds for the increased strain of the high temperature materials; for these, the bimetallic precursor phase is more uniformly alloyed with less residual, unalloyed Cu[25], which effectively makes the alloy phase richer in Cu. We note that experimental as well as computational work suggest that particle-size (surface stress) induced lattice contraction in small Pt

particles becomes significant only below a particle diameter of 2.5 nm [37, 38] and can be therefore ruled out as source of strain for the dealloyed core shell particles.

To gain insight into how the strain of the dealloyed catalysts affects the catalytic surface reactivity, we studied the electronic band structure. The d-band model developed by Nørskov and coworkers has been successful in relating the adsorption properties of rate limiting intermediates in catalytic processes to the catalyst electronic structure [39-41]. For simple adsorbates, such as the ORR intermediates O and OH, this can be understood in a simple electron interaction picture where the adsorbate valence p-level forms bonding and antibonding states with the metal d-band [40, 41]. Population of any antibonding state will lead to Pauli repulsion, and the bond strength will thereby be weakened. A downward shift of the d-band will pull more of the antibonding states below the Fermi level, resulting in increasing occupation and weaker adsorbate bonding. We have extended and applied these ideas to single-crystal Pt surfaces by preparing and characterizing bimetallic single-crystal model surfaces consisting of atomic layers of Pt with varying thickness grown on a Cu(111) substrate. This model mimics the structural and electronic environment of Pt layers surrounding a particle core with significantly smaller lattice parameter, similar to the dealloyed Pt-Cu catalysts[42]. Fig 3A shows photoelectron spectra of the valence band of Pt in Pt(111) and for 5 ML Pt grown on Cu(111) measured at grazing electron emission to enhance the surface sensitivity. There is no detectable Cu signal in the 5ML Pt spectrum, and it thereby represents pure Pt with no ligand effect from the underlying Cu substrate. Based on Low Energy Electron Diffraction (LEED) probing of the lattice parameter during the growth of Pt on Cu(111), 5ML Pt should give of the order of 2.5±0.3% compressive strain as shown in SI Figure S6. The spectrum of Pt on Cu(111) shows a much broader d-band compared to the Pt(111) surface, and the d-band center is downshifted from 2.87 eV to 3.26 eV below the Fermi level. The broadening is directly related to the compressive strain, since the electronic state overlap between the metal atoms increases with shorter interatomic distances; further, keeping the d-occupancy constant for a pure metallic system gives rise to a downward shift of the d-band center[43]. Next, we use x-ray spectroscopy to directly monitor the position and atom-specific occupation of the O 2p- Pt 5d antibonding states projected onto the oxygen atom [40, 41]. Fig. 3B shows O K edge X-ray Emission (XES) and

X-ray absorption spectra (XAS) of atomic oxygen adsorbed on thin films of Pt on Cu(111) and Pt(111) probing the occupied and the unoccupied electronic states, respectively. For oxygen on Pt(111), we observe a broad occupied bonding state in the XES spectrum and an intense resonance related to the antibonding state in the XAS spectrum. For the two Pt films on Cu(111), corresponding to strains of around 2.8±0.3 % and 3.3±0.3 %[42], we observe a decrease in the intensity of the antibonding resonance with increasing strain. Of primary interest is that, for the film with maximum strain, the antibonding resonance vanishes in the XAS spectrum and is resolved in the XES spectrum, directly indicating that the antibonding state is fully occupied with a peak around 1.5 eV below the Fermi level.

In order to quantify the relationship between surface strain, O/OH binding energies, and the catalytic ORR reactivity, we carried out Density Functional Theory (DFT) calculations to predict the changes in the Pt-O surface bond energy for a strained Pt(111) model surface. Our computations show a linear relationship between lattice strain and the adsorbate bond energy, consistent with the experimental x-ray spectroscopy data and previous computational analyses[16, 44]. By combining the strain-bond energy relationships with a microkinetic model, originally developed by Nørskov et al.[39], for the electroreduction of oxygen [18, 45], we derive a "volcano" relation between the predicted ORR reaction rate and the strain, as shown in Figure 4. The volcano shape implies that compressive strain first enhances the overall ORR activity by reducing the binding energy of intermediate oxygenated adsorbates and, thereby, lowering the activation barriers for proton and electron transfer processes. Beyond a critical strain, however, the binding becomes too weak, and the catalytic activity is predicted to decrease due to an increased activation barrier for either oxygen dissociation or the formation of a peroxyl (OOH) intermediate[39].

In Figure 4, we have also plotted experimentally measured ORR electrocatalytic activities for our Pt-Cu catalysts as a function of s(Pt) (electrochemical currents are reported in SI Table S1). The fact that we do not observe a decrease in the experimental activity values on left side of the volcano curve, as predicted by theory, is likely related to compressive strain relaxation in the Pt shells. Pt atoms adjacent to the Pt-Cu cores (see point "2" in Fig. 2C) will adopt a lattice parameter closer to that of the cores[32], but outer

Pt shell atoms (point "1" in Fig. 2C) will relax towards the bulk Pt lattice constant[42]. Hence, the surface strain will be less than that represented by a_{shell}, which is an average strain in the Pt shell; if the surface strain were plotted in Fig. 4, we expect a shift of all experimental data points to the right. Additionally, we note that it is difficult to prepare dealloyed nanoparticles with sufficiently high surface strain to access the true maximum of the volcano; when the strain passes a critical point, surface relaxation is likely to relieve further strain and thereby limit the accessibility of the high-strain side of the volcano. Fig.4 also reveals that the activity of the set of dealloyed nanoparticle catalysts prepared at the higher annealing temperature exhibit reduced activity at comparable lattice strain in the particle shells, presumably due to differences in the mean particle size. Our strain-related conclusions hence generally refer to particles of comparable size.

Discussion

Dealloyed fuel cell catalysts show unprecedented electrocatalytic activity for the electroreduction of oxygen, yet a fundamental understanding of the mechanistic origin of the catalytic enhancement was missing. With the present work, we have clarified the atomic-scale origin of the exceptional electrocatalytic activity of dealloyed Pt-Cu nanoparticles. We have presented microscopic and spectroscopic evidence for the formation of a Pt-Cu alloy core-Pt shell nanoparticle structure using STEM elemental maps (Fig.1), XPS depth profiling (Table 1), and ASAXS[33]. Given the thickness of the pure Pt shell and considering the limited range of ligand effects[46], we have concluded that compressive strain effects rather than ligand effects are responsible for the exceptional reactivity of the particle surface; this is in contrast to other ORR electrocatalyst systems, such as Pt monolayer[20] or Pt skin[17] catalysts, where strain and ligand effects are always convoluted. Using X-ray diffraction, we have measured and quantified the presence of compressive lattice strain in the Pt shells of the dealloyed particles.

To further corroborate the lattice strain hypothesis in core-shell structures, we have studied a surface science core-shell model system. Our goal was to experimentally verify the predicted effects on the band structure for compressively strained Pt layers. In contrast to previous reports of reactivity-band structure correlations[19] in which band

broadening and band center shifts were adopted from computational predictions, we have experimentally demonstrated a continuous change of the O 2p- Pt 5d antibonding state from above to below the Fermi level as additional compressive strain is applied, resulting in a weakening of the adsorbate bond. This result represents the first direct experimental confirmation of the computational prediction of band shifts of adsorbate projected band structure. Finally, we have directly correlated experimental synthesis-strain-activity data of dealloyed core-shell particles (Fig. 4). The resulting activity-strain relations provide experimental evidence that the deviation of the Pt-shell lattice parameter from that of bulk Pt, that is the lattice strain in the shell, is the controlling factor in the catalytic enhancement of dealloyed Pt nanoparticles; in particular, they are consistent with computational predictions that compressive strain enhances ORR activity.

In conclusion, a coherent picture of the origin of the exceptional electrocatalytic reactivity for the ORR of dealloyed Pt-Cu particles has now been established. Strain forms in Pt enriched surface layers (shells) which are supported on an alloy particle core with a smaller lattice parameter. The compression in the shell modifies the d-band structure of the Pt atoms, thereby weakening the adsorption energy of reactive intermediates compared to unstrained Pt and resulting in an increase in the catalytic reactivity, consistent with DFT-based predictions. A unique feature of the class of dealloyed catalysts is the experimental control over the extent of dealloying (shell thickness) and the alloy core composition (the upper limit for strain in the shell). The noble and the non-noble constituents can be adjusted in the alloy precursor, such that both expansive and compressive strain can be achieved for the purpose of controlled strengthening or weakening surface bonds. This enables a continuous tuning of catalytic reactivity. We have explicitly demonstrated such strain-related tuning for the ORR, and we note that this phenomenon is likely to offer control over the activity of other important electrocatalytic reactions which require modification of the adsorption energy of reactive intermediates, such as the electrooxidation of small organic molecules, including ethanol, methanol, and related species.

Methods

Synthesis. Pt-Cu binary electrocatalysts precursors were synthesized using a liquid metal-salt precursor impregnation method followed by freeze-drying and thermal annealing. This method has been previously applied for the synthesis of binary[25, 47] and ternary[24] Pt alloys. The nanoparticle catalyst precursors were prepared by adding appropriate stoichiometric amounts of a solid Cu-precursor ($Cu(NO_3)_2$ 2.5H$_2$O, Sigma-Aldrich) to weighted amounts of commercial Pt electrocatalyst powder, of 30 wt% platinum nanoparticles supported on high-surface-area carbon (TEC10E30E from Tanaka Kikinzoku Inc., Japan).

Electrochemical Measurements. The voltammetric response of the electrocatalysts was first measured during the initial three CV scans of 100 mV/s to obtain the initial rapid Cu dissolution profiles. The catalysts were further pretreated using 200 CV scans between 0.05 V and 1.0 V at a scan rate of 500 mV/s during which a large amount of Cu was lost from the alloy nanoparticles. Thereafter, the platinum electrochemical surface area (Pt-ECSA) was determined by cycling the treated catalysts at 100 mV/s between 0.05 V to 1.2 V and integrating the faradaic charge associated with stripping of underpotentially deposited hydrogen (see SI Fig. S1A). Pt-ECSA measurements using CO stripping resulted in comparable values of the surface area.

Linear sweep voltammetry (LSV) measurements were conducted in oxygenated electrolyte, under O$_2$ atmosphere, by sweeping the potential from 0.06 V anodically to the open circuit potential (~ 1.0V) at the scan rate of 5 mV/s (see SI Fig. S1B). The ORR activities of the dealloyed, activated catalysts were corrected for mass transport limitation using equation (5) in ref. [3]. Mass and surface-area specific activities were then established at 900 mV at room temperature (see SI Fig. S1C,D).

Electron Microscopy (STEM) and Energy Dispersive Spectroscopy (EDX).
Energy-dispersive X-ray spectroscopy (EDS) spectrum imaging was performed in scanning transmission electron microscopy (STEM) mode at 200 kV with a Philips CM200FEG equipped with an EDAX detector/pulse processor and an Emispec Vision

system (see SI Fig. S2). Pt-L and Cu-K elemental maps were extracted from the spectral data and the Pt(blue)-Cu(red) color map overlays were made. Sub-Angstrom resolution high-angle annular dark-field (HAADF) STEM images of individual Pt-Cu nanoparticles were recorded using a JEOL 2200FS C_s-corrected STEM (CEOS hexapole aberration-corrector) operated at 200kV.

Anomalous X-ray Diffraction (AXRD). Synchrotron-based XRD was used to characterize Pt-alloy electrocatalyst precursor powders as well as electrochemically treated activated catalyst films using X-ray energies from 8900 eV, through the Cu K-adsorption edge (8979 eV), to 9150 eV. Diffraction measurements were conducted at the Stanford Synchrotron Radiation Lightsource (SSRL) beamline 2-1. A detailed description of the analysis of the AXRD results is provided in the SI.

Computational Methods. The computational analysis is performed using DACAPO[48], a total energy calculation code. All calculations are performed on a four-layer slab with a 2x2 unit cell. Full relaxation of the oxygen adsorbate and of the first two metal layers is allowed. For strained Pt slabs, uniform expansion (or contraction) of the Pt(111) lattice was allowed in all three Cartesian directions, and no corrections to the interlayer Pt distance are included. This model provides a reasonable representation of the compression that is found in the Pt-base metal alloys that form the substrate of the Pt samples.

X-ray Photoelectron Spectroscopy (XPS), X-ray Emission Spectroscopy (XES) and X-ray Absorption Spectroscopy (XAS). XPS, XES and XAS measurements were performed in an ultrahigh vacuum (UHV) endstation with a base pressure better than 10-10 Torr at beamline 13-2 at SSRL, which contains an elliptically polarized undulator that allows control of the direction of the photon E-vector about the propagation direction. An electron energy analyzer (VG-Scienta SES-100 or R3000) mounted perpendicular to the incoming light, was used for the XPS measurements. This is also equipped with a partial yield detector for X-ray absorption measurements. Samples were mounted on a rotatable sample rod in grazing angle (~5o) with respect to the incoming light. The independent

rotation of the sample and the photon polarization (E-vector) allowed for selection of arbitrary angles between the E-vector and the sample surface and any choice of detection angle with respect to the sample surface.

The XPS spectra were obtained at a photon energy of 620 eV with energy resolution better than 0.2 eV. Grazing emission XPS spectra were taken to enhance the surface contribution at an emission angle of 15° with respect to the sample surface. Oxygen XAS spectra were obtained with a retarding voltage of 400 eV to monitor the O KVV Auger electron yield. The XAS spectra were recorded with energy resolution better than 0.1 eV, and the photon E-vector was aligned parallel to the surface plane, referred as in-plane geometry. The XES spectra were taken in normal emission by a grazing incidence soft x-ray spectrometer using a 1100 line/mm elliptical grating giving a resolution of around 0.7 eV. This corresponds to probing the in-plane orbitals. The excitation energy for the XES spectra corresponds to excitations into the strong XAS resonance at 530 eV in order to eliminate any contributions of non-diagram transitions.

XPS analysis. Composition of the catalysts was determined by measuring the ratio of Pt4f to Cu3p XPS intensities normalized to their respective subshell photoionization cross sections[49] for different photon energies using the experimental set-up described above. The kinetic energy of photoelectron defines the inelastic mean free path (IMFP) and the probing depth of the analysis. We varied the photoelectron kinetic energy by changing the incident photon energy to obtain the composition at different probing depths (see Table 1). Estimated probing depths of composition are 0.6 nm, 1 nm, 1.5 nm, 1.8 nm and 7 nm at photon energies of 250 eV, 620 eV, 1130 eV, 1480 eV and 8000 eV[50] respectively. Table 1 summarizes the depth profile of the nanoparticle catalysts before and after dealloying process. The depth profile is consistent with results obtained earlier[25].

Acknowledgements

References

1.   Stonehart, P. Development of alloy electrocatalysts for phosphoric acid fuel cells (PAFC). *Appl. Electrochem.* **22**, 995-1001 (1992).

2.   Mukerjee, S. & Srinivasan, S. in Handbook of Fuel Cells - Fundamentals, Technology and Applications, Vol. 2. (eds. W. Vielstich, H.A. Gasteiger & A. Lamm) 502 (John Wiley, Chichester; 2003).

3.   Gasteiger, H.A., Kocha, S.S., Sompalli, B. & Wagner, F.T. Activity benchmarks and requirements for Pt, Pt-alloy, and non-Pt oxygen reduction catalysts for PEMFCs. *Appl. Catalysis B: Environmental* **56**, 9-35 (2005).

4.   Ertl, G., Knözinger, H., Schueth, F. & Weitkamp, J. Handbook of Heterogeneous Catalysis. (Wiley-VCH, Weinheim; 2008).

5.   Somorjai, G.A. Introduction to Surface Chemistry and Catalysis. (Wiley, New York; 1994).

6.   Sinfelt, J.H. Bimetallic Catalysts: Discoveries, Concepts, and Applications. (John Wiley & Sons, London; 1983).

7.   Maroun, F., Ozanam, F., Magnussen, O.M. & Behm, R.J. The Role of Atomic Ensembles in the Reactivity of Bimetallic Electrocatalysts. *Science* **293**, 1811-1814 (2001).

8.   Rodriguez, J.A. & Goodman, D.W. The nature of the metal metal bond in bimetallic surfaces. *Science* **257**, 897 (1992).

9.   Rodriguez, J.A. Physical and chemical properties of bimetallic surfaces. *Surf. Sci. Rep.* **24**, 223-287 (1996).

10.   Greeley, J., Norskov, J.K. & Mavrikakis, M. Electronic Structure and Catalysis on Metal Surfaces. *Annu. Rev. Phys. Chem.* **53**, 319-348 (2002).

11.   Hammer, B. & Nørskov, J.K. Electronic factors determining the reactivity of metal surfaces. *Surf. Sci.* **343**, 211-220 (1995).

12.   Ruban, A., Hammer, B., Stoltze, P., Skriver, H.L. & Nørskov, J.K. Surface electronic structure and reactivity of transition and noble metals. *J. Mol. Catal. A: Chem* **115**, 421 (1997).

13. Chen, S. et al. Enhanced Activity for Oxygen Reduction Reaction on Pt3Co Nanoparticles: Direct Evidence of Percolated and Sandwich Segregation Structures. *J. Am. Chem. Soc.* **130**, 13818-13819 (2008).

14. Chen, S. et al. Origin of Oxygen Reduction Reaction Activity on "Pt3Co" Nanoparticles: Atomically Resolved Chemical Compositions and Structures. *J. Phys Chem. C* **113**, 1109-1125 (2009).

15. Chen, M., Kumar, D., Yi, C.-W. & Goodman, D.W. The Promotional Effect of Gold in Catalysis by Palladium-Gold. *Science* **310**, 291-293 (2005).

16. Mavrikakis, M., Hammer, B. & Norskov, J.K. Effect of Strain on the reactivity of metal surfaces. *Phys. Rev. Lett.* **81**, 2819-2822 (1998).

17. Stamenkovic, V.R. et al. Improved Oxygen Reduction Activity on Pt3Ni(111) via Increased Surface Site Availability *Science* **315**, 493 (2007).

18. Stamenkovic, V. et al. Changing the activity of electrocatalysts for oxygen reduction by tuning the surface electronic structure. *Angew. Chem. Int. Ed.* **45**, 2897-2901 (2006).

19. Kibler, L.A., El-Aziz, A.M., Hoyer, R. & Kolb, D.M. Tuning reaction rates by lateral strain in a palladium monolayer. *Angew. Chem. Int. Ed.* **44**, 2080-2084 (2005).

20. Zhang, J., Vukmiovic, M.B., Xu, Y., Mavrikakis, M. & Adzic, R.R. Controlling the Catalytic Activity of Platinum-Monolayer Electrocatalysts for Oxygen Reduction with different substrates. *Angew. Chem. Int. Ed.* **44**, 2132 (2005).

21. Oppenheim, I.C., Trevor, D.J., Chidsey, C.E.D., Trevor, P.L. & Sieradzki, K. In Situ Scanning Tunneling Microscopy of Corrosion of Silver-Gold Alloys. *Science* **254**, 687-689 (1991).

22. Erlebacher, J., Aziz, M.J., Karma, A., Dimitrov, N. & Sieradzki, K. Evolution of nanoporosity in dealloying. *Nature* **410**, 450-453 (2001).

23. Renner, F.U. et al. Initial Corrosion observed on the atomic scale. *Nature* **430**, 707-710 (2006).

24. Srivastava, R., Mani, P., Hahn, N. & Strasser, P. Efficient Oxygen Reduction Fuel Cell Electrocatalysis on Voltammetrically De-alloyed Pt-Cu-Co Nanoparticles. *Angew. Chem. Int. Ed* **46**, 8988-8991 (2007).

25. Koh, S. & Strasser, P. Electrocatalysis on bimetallic surfaces: Modifying catalytic reactivity for oxygen reduction by voltammetric surface de-alloying. *J. Am. Chem. Soc.* **129**, 12624-12625 (2007).

26. Strasser, P. in Handbook of Fuel Cells:Advances in Electrocatalysis, Materials, Diagnostics and Durability, Vol. Volumes 5 & 6. (eds. W. Vielstich, H.A. Gasteiger & H. Yokokawa) 30-47 (John Wiley & Sons Ltd, Chichester, West Sussex, UK; 2009).

27. Strasser, P., Koh, S. & Greeley, J. Voltammetric Surface Dealloying of Pt bimetallic nanoparticles: An experimental and DFT computational analysis. *Phys. Chem Chem. Phys.* **10**, 3670-3683 (2008).

28. Koh, S., Hahn, N., Yu, C. & Strasser, P. Effects of Compositions and Annealing Conditions on the Catalytic Activities of Pt-Cu Nanoparticle Electrocatalysts for PEMFC. *J. Electrochem. Soc.* **155**, B1281-1288 (2008).

29. Vielstich, W., Lamm, A. & Gasteiger, H. (eds.) Handbook of Fuel Cells - Fundamentals, Technology, and Applications. (Wiley, Chichester, UK; 2003).

30. Janik, M.J., Taylor, C.D. & Neurock, M. First-Principles Analysis of the Initial Electroreduction Steps of Oxygen over Pt(111). *J. Electrochem. Soc.* **156**, B126-B135 (2009).

31. Subramanian, P.R. & Laughlin, D.E. in Binary Alloy Phase Diagrams, Vol. 2, Edn. 2. (ed. T.B. Massalski) 1460-1462 1990).

32. Wang, J.X. et al. Oxygen Reduction on well defined Core Shell Nanocatalysts: particle Size, Facet and Pt Shell Thickness Effects. *J. Am. Chem. Soc.* **131**, 17298-17302 (2009).

33. Yu, C., Koh, S., Leisch, J., Toney, M.T. & Strasser, P. Size and composition distribution dynamics of alloy nanoparticle electrocatalysts probed by anomalous Small Angle X ray Scattering (ASAXS). *Faraday Discuss.* **140**, 283-296 (2008).

34. Cullity, B.D. & Stock, S.R. Elements of X ray diffraction, Edn. 3. (Prentice Hall, New York; 2001).

35. Pecharsky, V. & Zavalij, P.Y. Fundamentals of Powder Diffraction and Structural Characterization of Materials. (Springer, New York; 2003).

36. DeGraef, M. & McHenry, M.E. Structure of Materials: An Introduction to Crystallography, Diffraction, and Symmetry. (Cambrige University Press, Cambridge; 2007).

37. Klimenkov, M. et al. The structure of Pt-aggregates on a supported thin aluminum oxide film in comparison with unsupported alumina: a transmission electron microscopy study. *Surf.Sci.* **391**, 27-36 (1997).

38. Cammarata, R.C. Surface and Interface Stress effects in thin films. *Prog. Surf. Sci.* **46**, 1-38 (1994).

39. Hammer, B. & Nørskov, J.K. Why gold is the noblest of all metals. *Nature* **376**, 238-240 (1995).

40. Nilsson, A. et al. The electronic structure effect in heterogeneous catalysis. *Catal. Lett.* **100**, 111-114 (2005).

41. Nilsson, A., Pettersson, L.G.M. & Nørskov, J.K. Chemical Bonding at Surfaces and Interfaces. (Elsevier, Amsterdam; 2008).

42. Fusy, J., Meneaucourt, J., Alnot, M., Huguet, C. & Ehrhardt, J.J. Growth and reactivity of evaporated platinum films on Cu(111): a study by AES, RHEED and adsorption of carbon monoxide and xenon. *Appl. Surf. Sci.* **93**, 211-220 (1996).

43. Bligaard, T. & Nørskov, J.K. in Chemical Bonding at Surfaces and Interfaces. (eds. A. Nilsson, L.G.M. Pettersson & J.K. Nørskov) (Elsevier, 2008).

44. Lischka, M., Mosch, C. & Gross, A. Tuning catalytic properties of bimetallic surfaces: Oxygen adsorption on pseudomorphic Pt/Ru overlayers. *Electrochim. Acta* **52**, 2219-2228 (2007).

45. Norskov, J.K. et al. Origin of the Overpotential for Oxygen Reduction at a Fuel-Cell Cathode. *J. Phys. Chem. B* **108**, 17886-17892 (2004).

46. Schlapka, A., Lischka, M., Groß, A., Käsberger, U. & Jakob, P. Surface Strain versus Substrate Interaction in Heteroepitaxial Metal Layers: Pt on Ru(0001). *Phys. Rev. Lett.* **91**, 016101 (2003).

47. Mani, P., Srivastava, S. & Strasser, P. Dealloyed Pt-Cu Core-Shell Nanoparticle Electrocatalysts for use in PEM Fuel Cell Cathodes. *J. Phys. Chem. C* **112**, 2770-2778 (2008).

48. Hammer, B., Hansen, L.B. & Nørskov, J.K. Improved adsorption energetics within density-functional theory using revised Perdew-Burke-Ernzerhof functionals. *Phys. Rev. B* **59**, 7413-7421 (1999).

49. Yeh, J.J. & I.Lindau *Atomic Data and Nuclear Data Tables* **32**, 1-155 (1985).

50. Inelastic mean free paths of Pt 4f and Cu 2p photoelectrons in adlayer platinum matrix were estimated from the TPP2M formula in: S. Tanuma, C. J. Powell, D. R. Penn, Surf. Interf. Anal., Vol. 21, 165 (1993)

Figure Captions

Figure 1:

A), B) High-resolution Energy Dispersive Spectroscopy (EDS) elemental maps of a $Pt_{25}Cu_{75}$ bimetallic nanoparticle alloy precursor sample (A) and of the active electrocatalyst after Cu dealloying from the precursor (B). Pt is plotted in blue, Cu in red, pink domains indicate well-alloyed Pt-Cu domains. The precursor alloy was prepared at 800 °C and is supported on a high surface area carbon black. The dealloyed catalyst was obtained by voltammetric cycling of the precursor between 0.05 V and 1.2 V/ RHE in 0.1 M $HClO_4$ solution. Pt-Cu alloy domains are discernible in the centers of the dealloyed particles with a Pt-enriched surface. EDS elemental maps were acquired using a probe-corrected STEM and were extracted from spectrum images acquired from an area measuring 40nm X 40nm, with a beam size of ~0.2nm and a step (pixel) size of ~0.2nm.

C) High-resolution EDS line profile (intensity (cps) vs. distance (nm)) across an individual ~4nm diameter dealloyed Pt-Cu alloy active catalyst particle. Data were acquired using a probe-corrected STEM with a probe diameter ~0.2nm and step size ~0.2nm). The thickness of the Pt-enriched particle shell is ~0.6nm, as shown by dashed lines in image.

D), E) Sub-Angstrom resolution HAADF-STEM images of individual (~4 nm) Pt-Cu nanoparticles showing a typical Pt-Cu precursor alloy nanoparticle (D) and a typical Pt-Cu dealloyed nanoparticle (E). The dealloyed nanoparticle exhibits an outer Pt-enriched shell (outer shell images brightly) and Pt-Cu alloy core (which images less brightly than the shell). Contrast variations in the HAADF-STEM images result from the atomic number (Z) difference between Pt and Cu – this is commonly referred to as Z-contrast imaging. The thickness of the Pt-enriched particle shell is ~0.6nm in image (E).

Figure 2:

A) Anomalous X-ray Diffraction (AXRD) intensity profiles of a $Pt_{25}Cu_{75}$ alloy precursor as function of the scattering vector Q. Diffraction profiles were taken as a function of the X-ray energy across the X-ray absorption edge of Cu at 8990 eV. Scattering intensities of Bragg reflections (shown are the (111) and (200) reflections) decrease as the Cu absorption edge energy is approached. The extent of intensity decrease is correlated with the Cu content of the scattering phase and can be used to extract composition.

B) Fitting the model equation (S2) for the scattering amplitude (black line) to experimentally measured values for the amplitude yield estimates for the molar fraction of Pt and Cu of the bimetallic material. AXRD provides the lattice parameter of the scattering phase (structural information) as well as its actual composition (chemical information).

C) Scheme of a simple two-phase structural model for the dealloyed state of a bimetallic particle. Pure Pt layers are surrounding one or more atomic layers of an alloy particle core. a_{shell} and a_{core} represent the mean lattice parameters in shell and core, respectively. Deviations of a_{shell} from the bulk unit cell parameter of pure Pt, a_{Pt}, imply strain s(Pt). Shell and core regions possess a fcc structure and are assumed to be structurally and compositionally uniform. Using a simple linear model, equation (S3), a_{shell} can be estimated without further assumptions about the volume of core or shell. Since Pt-Cu alloys exhibit unit cell parameters that are smaller than pure Pt, the model predicts a_{shell} < a_{Pt}, that is, compressive strain in the shell. Unlike the model, a real core-shell particle will show a gradient in lattice parameters with strain in the surface layer (point "1") being less than in layers near the core (point "2").

D) Determination of a_{shell} for dealloyed Pt-Cu bimetallics, plotted as a function of the alloy precursor Cu at% composition and its preparation temperature. Cu rich precursors display a smaller lattice parameter, as do higher annealed precursors. All alloys show lattice parameters below that of pure Pt (dotted line).

Figure 3:

A) Photoelectron spectra of the valence band region for Cu(111), Pt(111) and 5 ML of Pt on Cu(111) measured with a photon energy of 620 eV and with a 15° grazing electron emission angle. The inelastic background has been subtracted. The spectra of the 5ML Pt on Cu(111) is completely dominated by the emission from Pt since no sharp Cu d-band emission is seen at 2.3 eV from the under laying substrate and similar spectra is also seen for 3ML of Pt.

B) In-plane polarized O K edge x-ray absorption spectra (XAS) and normal emission O K edge x-ray emission spectra (XES) of 0.2 ML of oxygen chemisorbed on 3.6 ML and 2.6 ML films of Pt on Cu(111) and on bare Pt(111). The XAS have been normalized with respect to the high energy region where the cross section is dominated by atomic effects related to the photoionization continuum whereas the absolute intensity scaling between the XES and XAS spectra is arbitrary. The energy scale is with respect to the O 1s binding energy which represents the Fermi level[38]. The strain has been estimated based on the Pt coverage and using the LEED data shown in fig. S6.

Figure 4:

Experimental and computational relative surface-area based ORR activity

(in units of $kT \ln \dfrac{j_{s,alloy}}{j_{s,Pt}}$) of dealloyed Pt-Cu bimetallic nanoparticles plotted as a

function of strain, s(Pt), in the shell of dealloyed Pt-Cu core-shell nanoparticle
electrocatalysts. The y-axis is proportional to the logarithm of the ratio of the ORR
current density of the dealloyed particles to the ORR current density on unstrained Pt
nanoparticles; this quantity is the effective difference in ORR activation energies between
the strained and unstrained platinum surfaces. The experimental strain represents upper
bounds the nanoparticle surface strain. The black dashed line represents the DFT
predicted volcano-shaped trend of the ORR activity for a Pt(111) single crystal slab under
isotropic strain. Moderate compressive lattice strain is predicted to enhance the rate of
ORR catalysis. Triangles plot the experimental activity (see values in $\mu A/cm^2$ and
corresponding normalized values in SI Table S1) against the strain, s(Pt); the red and blue
triangles denote dealloyed Pt-Cu catalysts prepared at annealing temperatures of 800 °C
and 950 °C, respectively. The red and blue lines guide the eye; they emphasize the trend
that compressive lattice strain controls catalytic ORR activity for each catalyst, in accord
with DFT predictions. The activity of unstrained Pt is defined to be zero for both the
theoretical and experimental data. The plotted ORR activities used T= 298 K.

Table 1:

Composition depth profiles for Pt25Cu75 nanoparticles catalysts annealed at 950 °C
before and after dealloying. Increasing photon energy correlates with increased probing
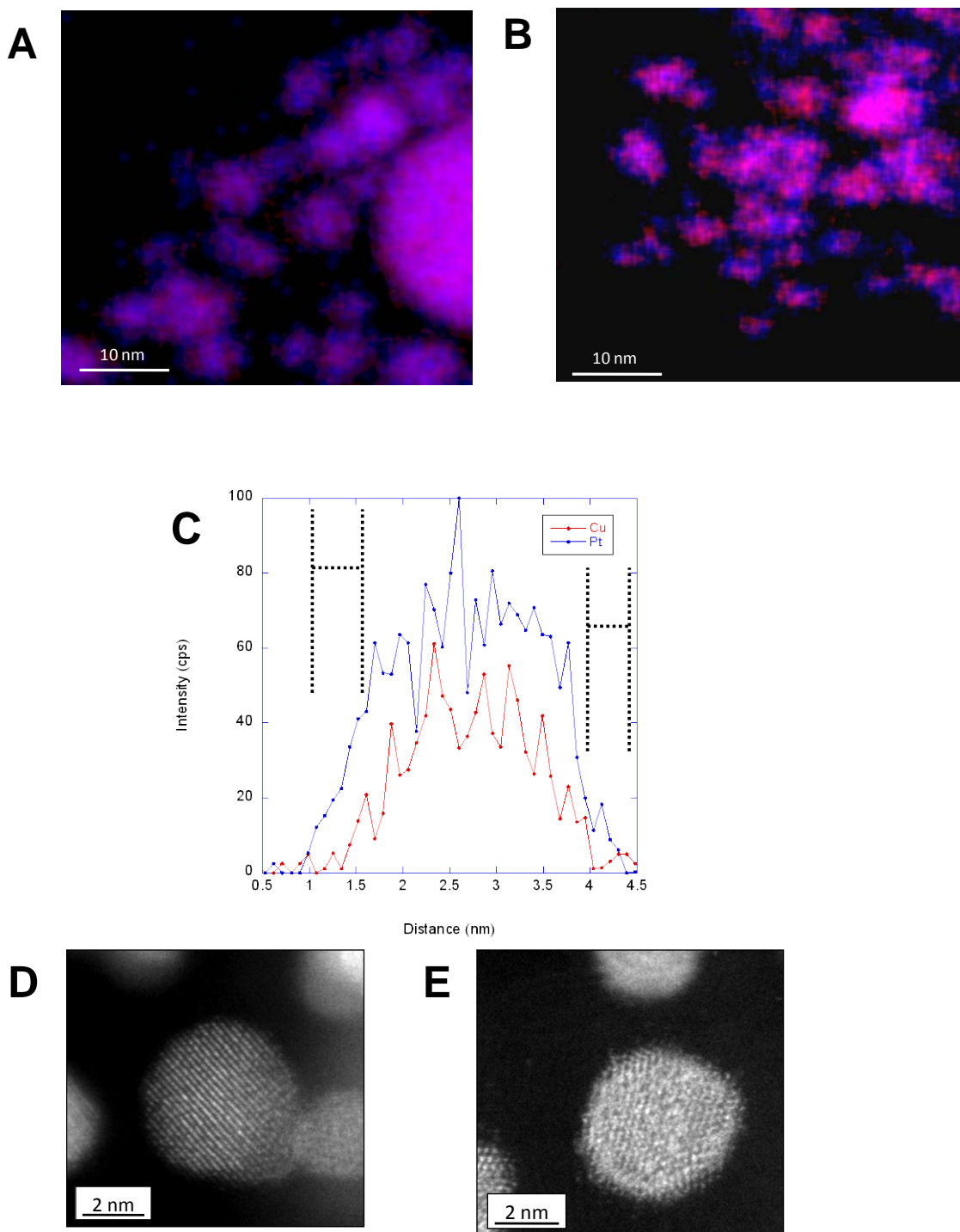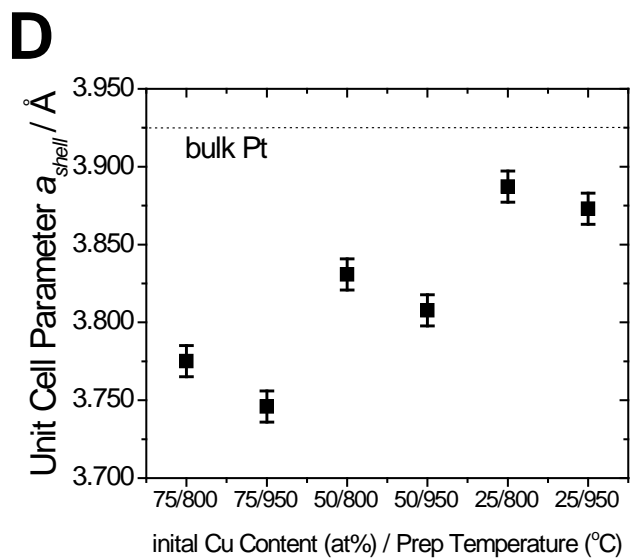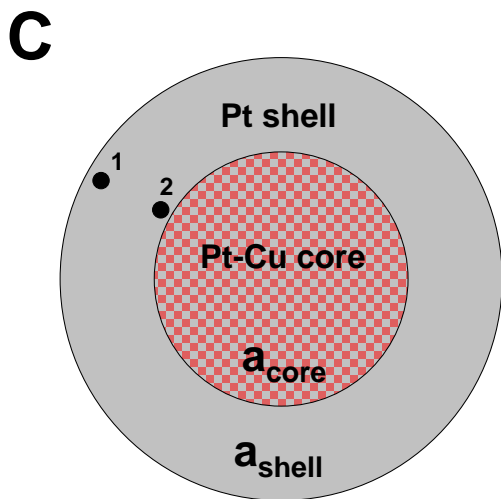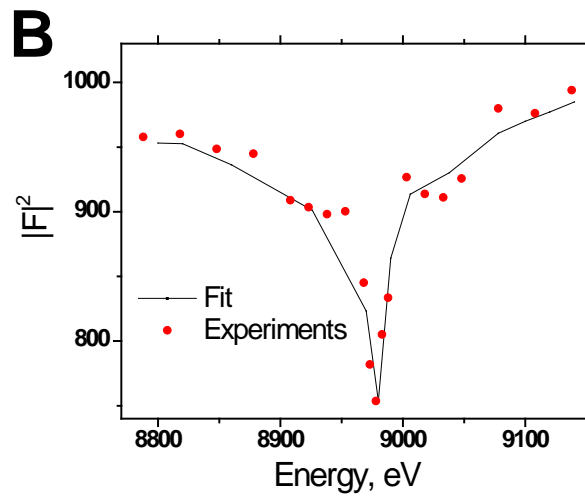depth.

Figure 1

A

B

C

D

Figure 2

A

PES
hν = 620 eV

e⁻ 15°

— 5ML Pt/Cu(111)
— Pt(111)

Cu(111)

Intensity (arb. units)

Binding Enegy (eV)

8   6   4   2   0

B

XES   AdsorbedO   XAS
        Bonding   Antibonding

Strain   Pt/Cu(111)

3.3%   2.6 ML

2.8%   3.5 ML

0%   Pt(111)

Intensity (arb. units)

Binding Enegy (eV)

10   5   0   -5
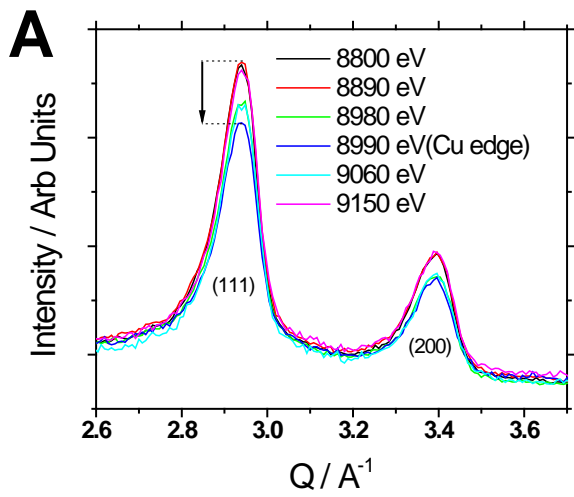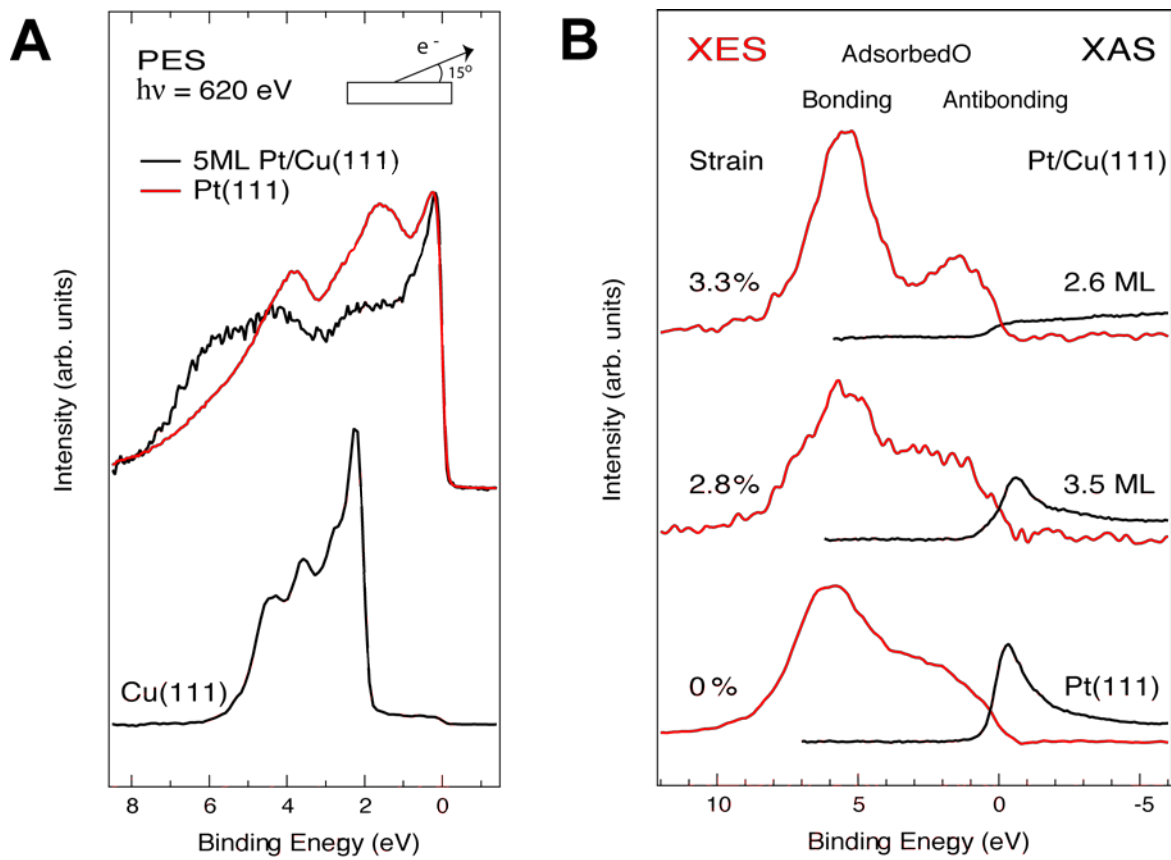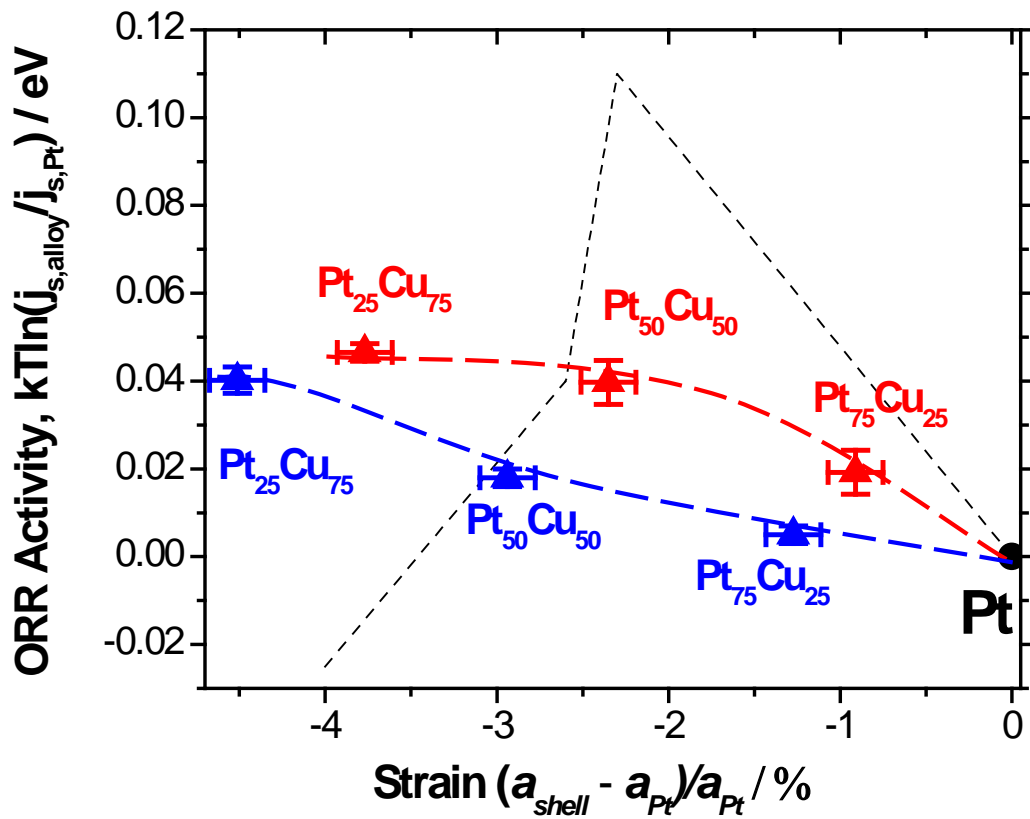
Figure 3

Figure 4

Platinum content at %					
Photon energy (eV)	264	616	1133	1480	8000
$Pt_{25}Cu_{75}$ precursor	8	12	19	18	31
$Pt_{25}Cu_{75}$ dealloyed	84	68	55	56	59

Table 1